1 Supporting information for "**Multimodal spectroscopic investigation of the**

2 **conformation and local environment of biomolecules at an electrified interface**"

3 Sasha A. Moonitz, Noah Shepard, Rodrigo Noriega

4 *University of Utah, Department of Chemistry, 315 S. 1400 E.*

5 *Salt Lake City, UT 84112*

6 Email: noriega@chem.utah.edu; phone: (801) 579-7979

7 <u>**Contents**</u>

22 **Materials and sample preparation.** Details on the deposition of ITO films, preparation

23 of buffers and sample solutions are provided below.

24 *Deposition of ITO films.* The optoelectronic properties of magnetron sputtered ITO thin

25 films are strongly dependent on processing conditions.[1–5] Our sensors were grown on

26 clean sapphire substrates (double-side polished, c-cut, 2.54 cm x 2.54 cm x 0.5 mm,

27 University Wafer) via DC magnetron sputtering (Denton Discovery 18) at room

28 temperature and with a DC power of 50 W. The vacuum chamber was evacuated to

29 1.9×10^{-6} Torr before it was pumped with a 99:1 argon/oxygen gas mixture to

30 4.34×10^{-3} Torr. Deposition was carried out for a variable time period to achieve desired

31 film thickness. After deposition, ITO films were annealed ex-situ under nitrogen gas in a

32 rapid thermal annealing oven (Allwin AccuThermo AW610) at a temperature of 350° C for

33 2 minutes. The resulting ITO films have a low surface roughness (**Fig. S1**), with a

34 maximum root-mean-square value (R_q) of 2.15 nm – most substrates have $R_q \sim$ 1 nm.
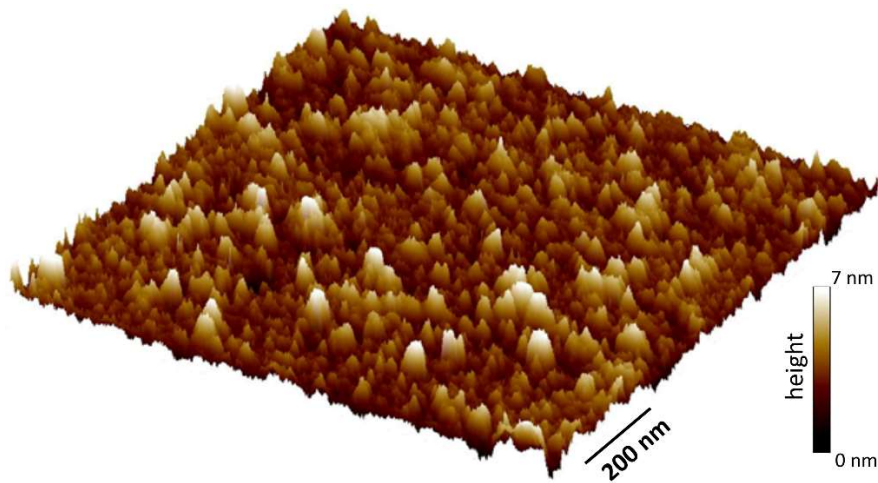
Figure S1. **Atomic force microscopy image** shows the topography of a representative section
(1 μm x 1 μm) of a sputtered ITO film, with R_q = 0.93 nm.

35 *Buffer solutions.* Britton-Robinson buffer (BRB) solutions were prepared at pH=7 and

36 pH=11 and constant ionic strengths (50 mM - 1.5 M).[6] Equimolar amounts of phosphoric

37 acid (Sigma-Aldrich CAS 7664-38-2), glacial acetic acid (Sigma-Aldrich CAS 64-19-7),

38 and boric acid (Fisher Scientific CAS 10043-35-3) were dissolved in HPLC grade water.

39 For pH=11 buffers, 4.1 mM of each acid were used; 4.5 mM were used for pH=7 buffers.

40 The pH of each buffer was monitored with a temperature calibrated pH probe

41 (Fisherbrand Accumet AE150) and 0.1 M sodium hydroxide was added until the desired

42 pH was obtained. The ionic strengths of each solution were determined by accounting for

43 the ionic product of water, the formal concentrations of each acid and sodium hydroxide

44 at each pH, using the acid dissociation constants (**Table S1**) to determine the fractional

45 compositions of each ionic species at each pH. NaCl was used to maintain a constant

46 ionic strength between buffers.

Acid	K_1	K_2	K_3
Acetic	1.754×10^{-5}	–	–
Phosphoric	6.92×10^{-3}	6.17×10^{-8}	4.786×10^{-13}
Boric	5.37×10^{-10}	3.98×10^{-13}	5.01×10^{-14}

47 **Table S1.** Acid dissociation constants used to determine fractional compositions of ionic species
48 present in Britton-Robinson buffers of varying pH.[7]

49 _Polypeptide solutions._ Poly-L-lysine hydrochloride (PLL, Sigma-Aldrich

50 CAS # 26124-78-7, m.w. > 30 kDa) was dissolved in pH 11 BRB solutions at a

51 concentration of 1 mg/mL and used for adsorption to the ITO surface. For samples used

52 in fluorescence experiments, an identical procedure was employed but with fluorescein

53 isothiocyanate labelled poly-L-lysine (FITC-PLL, Sigma-Aldrich SKU P3069, m.w. 30 –

54 70 kDa).

55 **Optical characterization of ITO films.** Spectroscopic ellipsometry measurements were

56 conducted immediately after film deposition. This allowed validation of successful thin film

57 deposition prior to incorporation into electrochemical, fluorescence, or plasmonic

58 experiments. To avoid artifacts in the data, the back side of the substrate was sanded

59   into a diffusive surface. Due to the destructive nature of this characterization step, a

60   sacrificial glass substrate was added to all film deposition runs. Data was collected with

61   a J.A. Woollam variable-angle spectroscopic ellipsometry (VASE) instrument; analysis

62   was performed with the instrument's onboard analysis software. Standard materials

63   parameters were used for Cauchy models of the glass substrate and air interface. A

64   Drude model was employed for the ITO film.[8–10] The ITO film thickness was allowed to

65   vary in the fitting routine, and thickness values were in agreement with profilometry

66   measurements. Materials parameters obtained for ITO films were a plasma frequency

67   $\omega_p = 2.2 - 3.1 \times 10^{15}$ Hz and damping coefficient $\Gamma = 2.5 \times 10^{14}$ Hz. These plasma

68   frequencies correspond to a free carrier density $n_e = 0.5 - 1.1 \times 10^{21}$ cm^{-3}. A typical

69   spectroscopic ellipsometry data set is shown in **Fig. S2**.
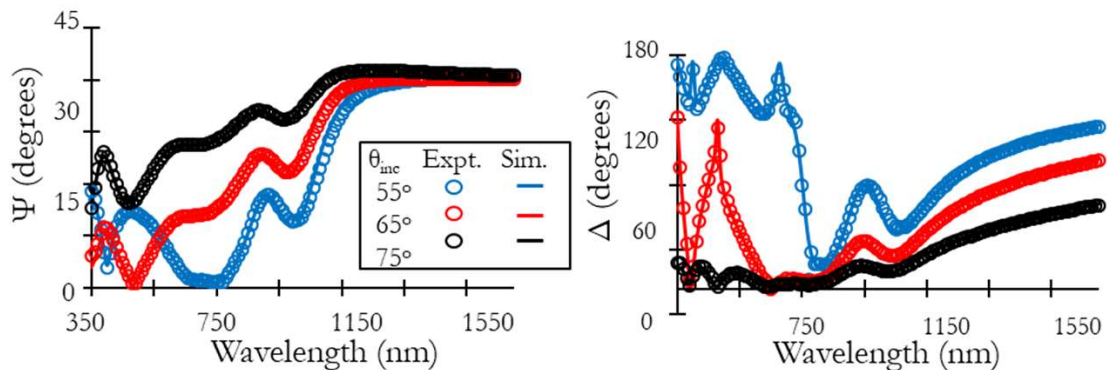
Figure S2. **Spectroscopic ellipsometry measurements on glass/ITO/air film stacks** can determine the optical constants of sputtered ITO films, which are then fit to a Drude model.

70   **SPR experimental setup.** Reflectivity as a function of incidence angle was measured

71   using CW and pulsed light sources (4.5 mW of λCW=1550 nm Thorlabs LDM1550; or

72   100-200 μW of λfs=2500 nm from a TOPAS Prime OPA pumped by a Coherent Astrella,

73   5 kHz repetition rate, 40 fs pulse duration). Incident light was directed to the SPR chips

74   using SF11 right-angle coupling prisms glued to the back side of the sapphire substrate

75   with UV-cured high refractive index epoxy (Norland NOA170). Fully assembled SPR chips

76   were mounted onto a homebuilt flow cell made with chemically resistant material (Kel-F)

77   and placed on a rotation stage; detection optics are mounted on a concentric rotation

78   stage for θ-2θ scans. The *p*-polarized incident light was focused onto the SPR chip

79   through the coupling prism with a Au spherical mirror with *f*=125 mm focal length. The

80   reflected beam was measured with a biased InGaAs photodiode (Thorlabs DET10D2)

81   whose output was fed to a lock-in amplifier (Ametek Signal Recovery) interfaced via a

82   data acquisition card (National Instruments). A beam chopper is included in the SPR line

83   to enable lock-in detection, and a sapphire beam sampler is used to split off a small

84   portion of the incident beam, which is directed to an identical detection setup as the

85   reflected beam and serves as a reference to eliminate fluctuations in laser power.

86   **Modeling of SPR response and sensitivity estimation.** Modeling of surface plasmon

87   resonances was performed using the Winspall software package by Res-Tec, which

88   employs the Fresnel formalism to calculate reflectivity curves of a planar film stack with

89   dielectric properties and thicknesses that are either user-defined or least-squares fitted

90   to data. When performing a fitting routine, only parameters corresponding to the ITO layer

91   were allowed to vary; material properties for sapphire, SF11 glass, air, water, and

92   methanol were fixed at reported literature values.[11–15] A small (<2 deg.) systematic

93   deviation in experimental vs. predicted angles is due to an offset in the rotation axis and

94   geometric center of the prism-substrate assembly, as well as minor angular deviations

95   during prism mounting. After fitting the thickness and dielectric properties of the ITO film

96   using their SPR response over a wide range of angles and in contact with multiple

97   dielectric media, these parameters were fixed for constant-angle SPR reflectivity

98   measurements.

99   Using the change in the SPR response for the same ITO film and different dielectric

100   media, it is possible to estimate the sensitivity of our experiments to changes in the

101   refractive index of the sample. Since probing condensed phases is the primary interest,

102   the SPR reflectivity at the ITO/H_2O and ITO/MeOH are compared. The difference in the

103   measured reflectivity $\Delta R = R_{\text{MeOH}} - R_{\text{H}_2\text{O}}$ is divided by the difference in the sample

104   refractive index $\Delta n = n_{\text{MeOH}} - n_{\text{H}_2\text{O}}$ to approximate the sensitivity $dR/dn \approx \Delta R/\Delta n$. As

105   expected given the good agreement of individual reflectivity curves with Fresnel models,

106   observations and predictions for sensitivity match quite well (**Fig. S3**). The maximum

107   measured sensitivity is $\Delta R/\Delta n = 4.75$. Our setup can routinely measure reflectivity values

108   with a resolution better than 10^{-3}, which would correspond to resolvable changes in

109   refractive index of 2×10^{-4} or better.
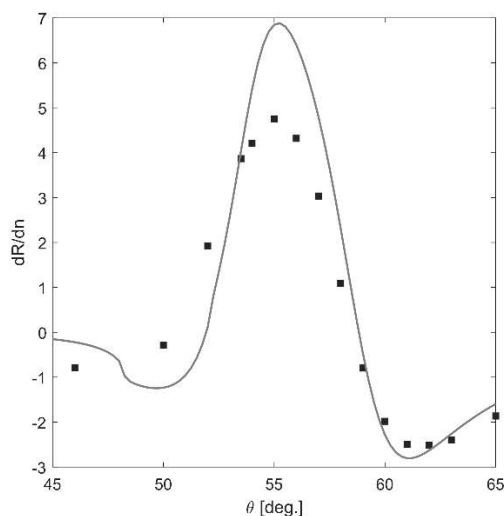
Figure S3. **Estimation of the SPR sensitivity** by considering the difference in reflectance for two simple dielectric media (water and methanol) measured sequentially in the same ITO SPR chip. The difference in reflectivity divided by the difference in refractive index is shown (experimental data as markers, model as continuous line).

110   **Electrochemical flow cell setup.** ITO chips were mounted in a custom three-electrode

111   electrochemical flow cell (**Fig. S4**) driven by a bipotentiostat (CH Instruments CHI700E).

112   The ITO sensors could be either mounted freely (TRPL) or bonded to a high refractive

113   index prism (SPR). Copper tape was adhered to the surface of the ITO thin film, enabling

114   its wiring as the working electrode. A 2 mm diameter platinum wire served as the counter

115   electrode. A 2 mm diameter Ag wire was soaked in a sodium hypochlorite solution and

116   used as a quasi-reference electrode (QRE). The open circuit potential of the Ag QRE was

117   measured against a Ag/AgCl reference electrode (CH Instruments CHI111) and found to

118   maintain a potential of -67 mV in saturated KCl solutions. During potential-driven

119   adsorption experiments, voltage was applied to the ITO working electrode for 15 minutes,

120   after which the SPR signal was recorded and compared to the reference signal when no

121   potential was applied. The sample solution was then flowed and the adsorption and data

122   collection procedure were repeated for all potentials studied. Time-resolved

123   photoluminescence studies examined the fluorescent signal of FITC-PLL already

124   adsorbed on an ITO substrate.
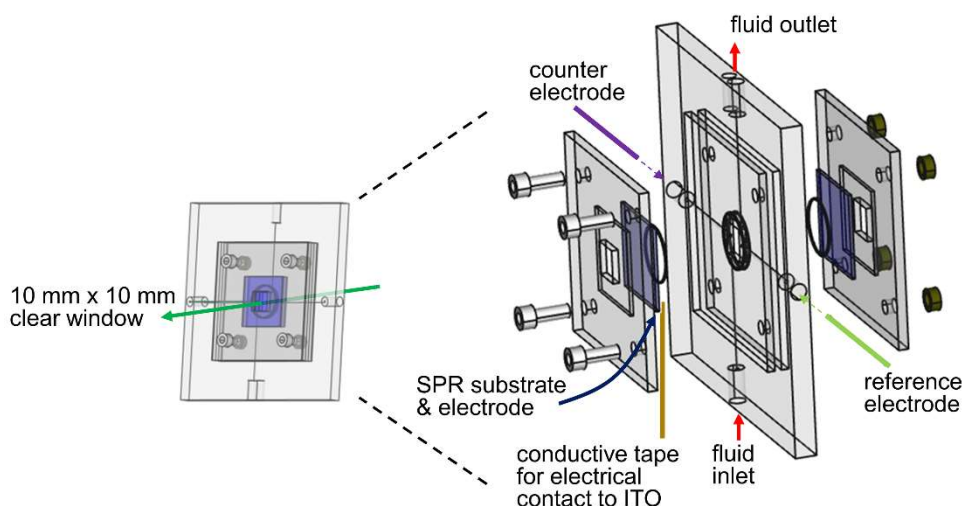
Figure S4. **Assembly of our electrochemical flow cell** designed to couple electrochemical and spectroscopic characterization of interfacial processes. Wiring connecting the working (ITO), counter (Pt), and reference (Ag/AgCl) electrodes to the bipotentiostat is not shown.

Time- and polarization-resolved fluorescence of polypeptide adsorbates. Excitation pulses were 150 μW of 490 nm excitation from the second harmonic of a tunable Ti:sapphire laser (Coherent Chameleon Ultra II, 80 MHz, <200 fs pulse duration) directed to the sample with a 530 nm long-pass dichroic, then focused with a single 75 mm focal length aspheric lens. Fluorescence was collected with the same lens, filtered with the long-pass dichroic and an additional long-pass filter (580 nm cutoff). Fluorescence was split into two orthogonal polarization channels and directed with large core optical fibers to identical single-photon Si photodiodes (MPD Systems) whose signal was routed to a TCSPC module (PHR 800 and Picoharp 300, PicoQuant). Data was acquired in a time-tagged time-resolved (T3) mode that incorporates full tagging of photon detection events with micro time (excitation-emission delay, 0-12.5 ns) and macro time (experimental frame for synchronization to stimuli). Identical ITO substrates were loaded onto a homebuilt flow cell; no SPR coupling prism was attached for these fluorescence experiments. A solution of FITC-PLL (1 mg/mL in pH 11.48 BRB, I=1.5 M) was flowed into the sample cell and the interfacial potential was stepped between -0.5–1.0 V to undergo the same adsorption monitored with SPR experiments. The sample cell was flushed with HPLC water several times to ensure that the only FITC-PLL remaining in the flow cell was that which had adsorbed to the ITO surface, as determined when no change in detected fluorescence was observed after 2 consecutive rinses (**Fig. S5**). Fluorescence data was collected for 15 minutes at each of the experimental conditions (pH, voltage) for which the first 2 minutes were in open circuit, then 12 minutes of applied potential, followed by 1 minute at open circuit. Buffer solution was flushed through for 5 minutes in between each set of experiments.
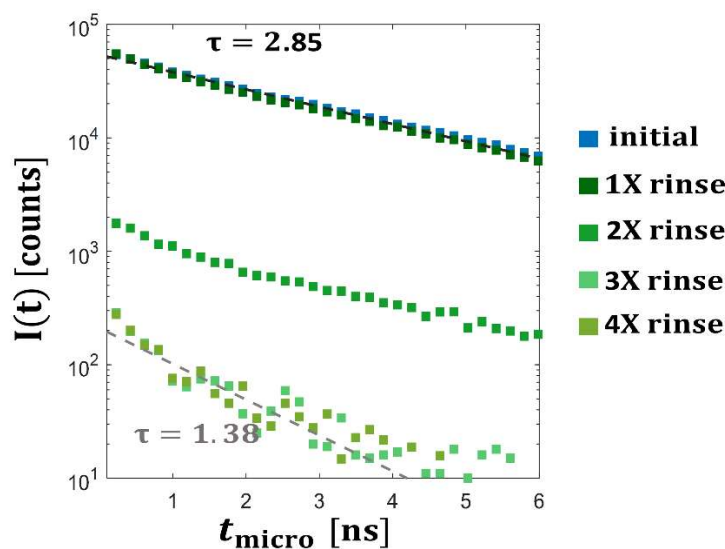
Figure S5. Fluorescence decay traces of FITC-PLL during adsorption and subsequent rinses show a decrease to a steady state corresponding to signal from the adsorbed film and not residual sample in solution. A substantial decrease in fluorescence lifetime is also observed for bulk vs. adsorbed species.

148 **Morphology of adsorbed polypeptide layer.** Following the electric-field assisted

149 deposition of PLL onto the ITO surface, atomic force microscopy reveals a partial

150 coverage of the ITO with PLL islands of variable height (**Fig. S6**). The volume fraction of

151 PLL, Φ_{PLL}, can be calculated using AFM height maps as the volume between the

152 topographical surface and the mean ITO baseline. For two nominally identical samples,

153 a layer height of 75-80 nm above the mean ITO level was obtained. In each of these

154 samples, the average PLL volume fraction over the entire AFM scans was Φ_{PLL}~3%.

155 However, considering the variability of coverage (**Fig. S6**), it is illustrative to calculate the

156 PLL volume fraction in the adhered layer within smaller regions (2x2 μm). With these local

157 averages, a noticeable population of regions with a PLL volume fraction Φ_{PLL}~8.5% can

158 be observed.
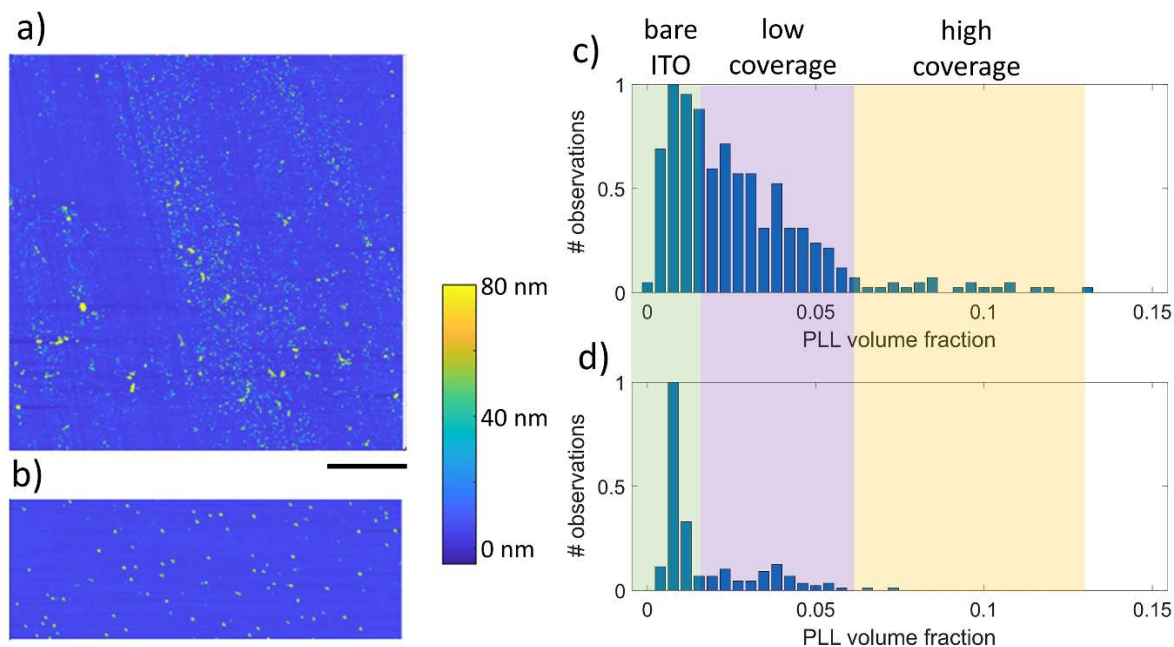
Figure S6. **Atomic force microscopy image of PLL adsorbates** atop ITO after electric-field assisted deposition from solution. Scale bar = 10 μm. Pseudo-color representations of the sample topography (on the same color scale) are shown on panels (a,b) on the left. A histogram of local PLL volume fractions (in 2x2 μm squares) for the two samples (a→ c, b→d). Shaded areas denote those regions with high ($\langle\Phi_{PLL}\rangle$~8.5%) and low ($\langle\Phi_{PLL}\rangle$~4%) PLL coverage, as well as those where mostly bare ITO is observed ($\langle\Phi_{PLL}\rangle < 1\%$).

159   **Assessing the hydration state of PLL adsorbates.** To model the SPR reflectivity upon

160   sample adsorption, an interfacial layer was inserted in the model atop the ITO surface

161   with a thickness (75-80 nm) and coverage (3-8.5%) that are representative of those

162   measured for PLL adsorbates (**Fig. S6**). With this geometry, the layer's thickness and

163   dielectric properties were optimized to match the observed change in reflectivity

164   (h=80 nm, $n_{boundary}$=1.304). If the refractive index of the mixed layer is approximated as

165   the weighted average of its components, the refractive index of the PLL adsorbates can

166   be estimated in the range n_{PLL}=1.8-2.7 (depending on the PLL volume fraction). This

167   range for n_{PLL} is in agreement with values reported for poly-alanine nanostructures

168   (n_{FFF}=1.53 @ 840 nm)[16], considering that the molar residue refractivity of lysine is twice

169   as large as that of alanine[17] and refractive indices decrease slowly at longer wavelengths

170   in the absence of resonances.

171   The small changes in reflectivity observed upon perturbation of the interface are easily

172   detected when the rotation stage and all detection optics are kept fixed. However, these

173   changes would be smaller than those resulting from positioning errors in the rotation

174   stage, which prevents the acquisition of full SPR curves as a function of continually

175   changing interfacial conditions. Thus, fixed-angle measurements provide useful

176   information regarding the interfacial layer but rely on assumptions on its properties – e.g.,

177   minimal changes in hydration while at constant pH. In this way, we account for the

178   average thickness of the adsorbed PLL layer assuming various hydration levels. For the

179   minimum (0.188) and maximum (0.193) values of reflectivity observed, average thickness

180   of the PLL adsorbed layer would be in the 175-200 nm range (adsorbates with 10%

181   hydration) or 210-235 nm range (adsorbates with 20% hydration).

182   **Fourier-transform infrared spectroscopy of PLL samples.** While the transparency

183   window of sapphire extends to ~ 6 μm, large path lengths through aqueous solutions

184   prevent the use of standard FTIR transmission measurements. To verify that our

185   polypeptide samples display the expected conformations in dry and solvated

186   environments, we performed FTIR absorbance experiments in transmission geometry for

187   dry PLL films atop blank sapphire substrates, and for concentrated PLL solutions in

188   methanol sandwiched between sapphire windows using a 6 μm spacer (**Fig. S7**). While

189   these conditions are different from those used in SPR and TRPL experiments, they

190   suggest that the poly-L-lysine samples used (~200 residues long chains) experience

191 similar conformational changes as those previously reported in the literature. Data were

192 collected with a Thermo Scientific Nicolet iS50 spectrometer (transmission configuration).
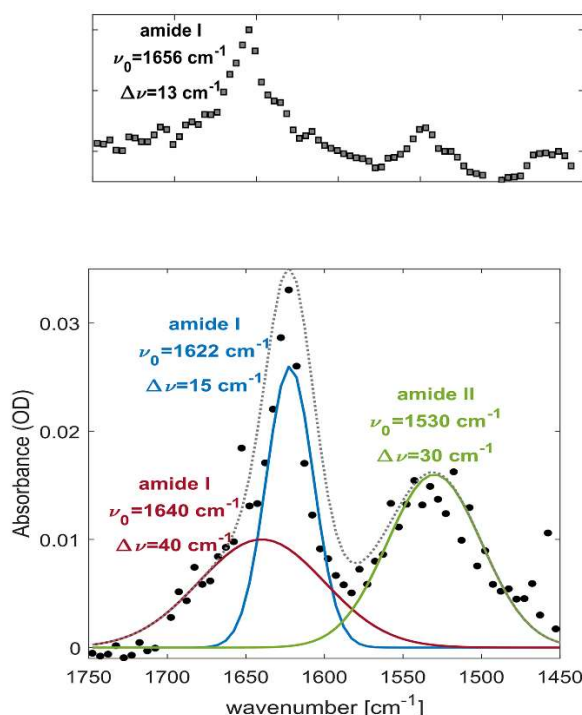
Figure S7. **FTIR spectra of dry PLL on sapphire** show peaks in the amide I and II regions. The amide I band can be used to assess secondary structure. In a dry film (bottom panel), peaks at 1622 cm⁻¹ and 1640 cm⁻¹ are characteristic of β-sheets. Top panel shows data for concentrated PLL solution in methanol with 63 mM of HCl, whose peak at 1656 cm⁻¹ is characteristic of α-helices.[16]

193 **Time-resolved fluorescence lifetime and anisotropy of polypeptide adsorbates at**

194 **an electrified solid/liquid interface.** The raw data for the TRPL experiments performed

195 in this work are photon detection events, tagged by channel (V or H polarization) and their

196 detection time (micro time and macro time). Binning these data by channel and macro

197 time allows for brightness trends. Histograms of micro time for a particular channel

198 contain fluorescence lifetime decay data. Differences in arrival time for each channel due

199 to different optical and/or electronic path lengths are accounted for with a horizontal shift.

200 Differences in collection efficiency for V/H polarization channels make it is necessary to

201 equalize the counts in these channels before calculating rotationally averaged

202   fluorescence decays traces and time-resolved fluorescence anisotropy. This is done by

203   the tail-matching method, where a specific sample is approximated as freely-diffusing

204   chromophore and its long-time values of V/H-polarized fluorescence are matched with a

205   scaling factor g for one of them so that the ensuing anisotropy decays to zero. Because

206   the V/H channel equalization factor g is an instrument variable, it is kept fixed for all other

207   samples. In our setup, $g=0.205$. The resulting rotationally averaged fluorescence decay

208   and time-resolved fluorescence anisotropy are given by **Eq. S1** and **S2**, respectively.

209     $$I_{tot}(t) = I_V(t) + 2g \cdot I_H(t) \quad \textbf{Eq. S1} \qquad\qquad r(t) = \frac{I_V(t) - g \cdot I_H(t)}{I_V(t) + 2g \cdot I_H(t)} \quad \textbf{Eq. S2}$$

210   The tail-matched data are binned as a function of macro time into 90 s periods, and the

211   micro time histograms for photons detected within that observation window are used to

212   compute fluorescence lifetime and time-resolved anisotropy traces, which are fitted as

213   single exponential decays with a nonlinear least-squares routine. Typical traces are

214   shown in **Fig. S8**. Due to the small amount of sample, the resulting count rates are low

215   (~35-150 cps) which prevented accurate determination of fitted parameters in a small

216   subset of data points (observations at t_{macro}>800 s in pH=7 at ΔV_{ITO}=750 mV and in pH=11

217   at ΔV_{ITO}=1 V, both for I=1.5 M).
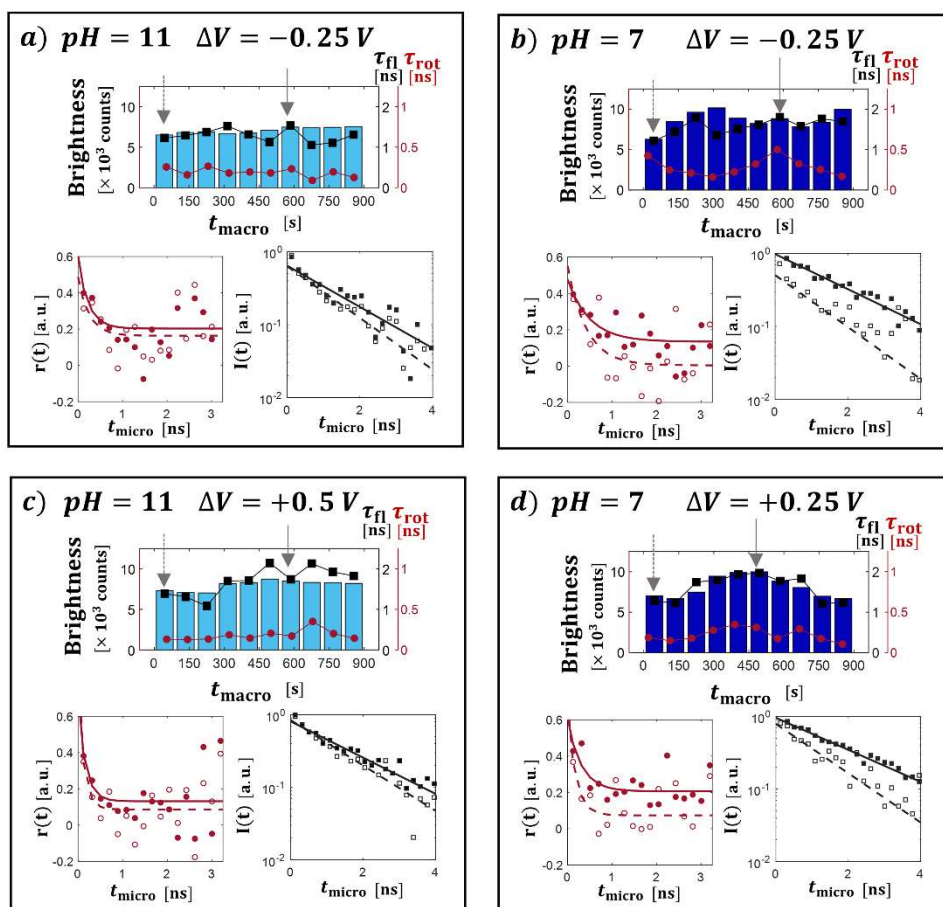
Figure S8. **Representative examples of time-resolved fluorescence I(t) and time-resolved fluorescence anisotropy r(t)** of FITC-PLL adsorbed on ITO substrates, as a function of the buffer pH and interfacial voltage. For each pH and ΔV set (a,b,c,d), two time points are chosen – one depicting the early dynamics before voltage is applied and another time point after the interfacial potential has been applied (denoted by gray arrows). The no-voltage dynamics are shown by empty markers (data) and dashed lines (fit); solid markers and solid lines depict the data and fit for the dynamics under applied voltage, respectively.

218   The correlation between brightness and photophysical parameters is supported by the

219   trends shown in **Fig. S9**. The sample brightness shows a clear positive correlation with

220   fluorescence lifetime τ_{fl} and with the asymptotic fluorescence anisotropy value $r(\infty)$.

221   Brightness does not show a noticeable correlation with either rotational diffusion time

222   scale τ_{rot} nor with the initial fluorescence anisotropy value $r(0)$.
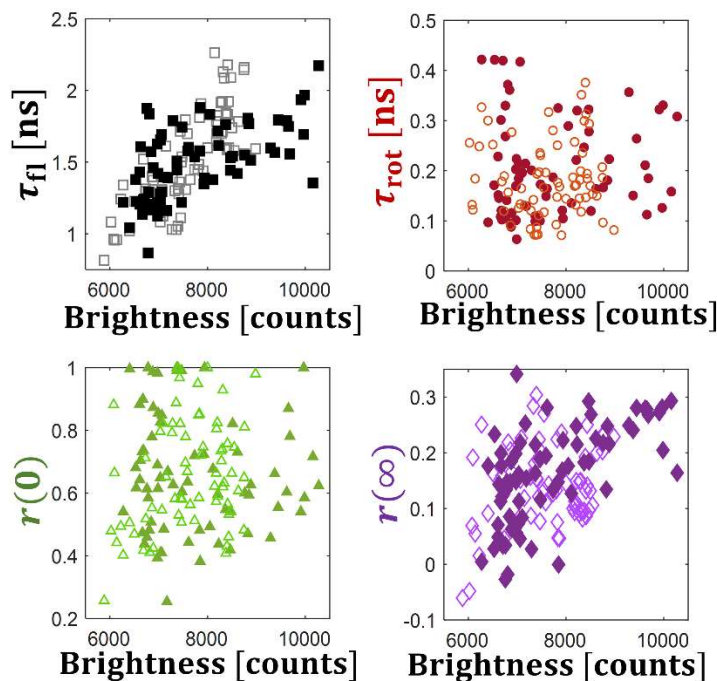
Figure S9. Fluorescence brightness shows a noticeable positive correlation with fluorescence lifetime and asymptotic anisotropy value, and no correlation with rotational diffusion time or initial anisotropy value. Filled markers correspond to data in pH=7 buffer, empty markers are pH=11 data.

223 The dependence of mean brightness and the presence of fluctuations as a function of

224 voltage display a discernible voltage trend at pH=11, and weak correlation with voltage at

225 pH=7 (**Fig. S10**).
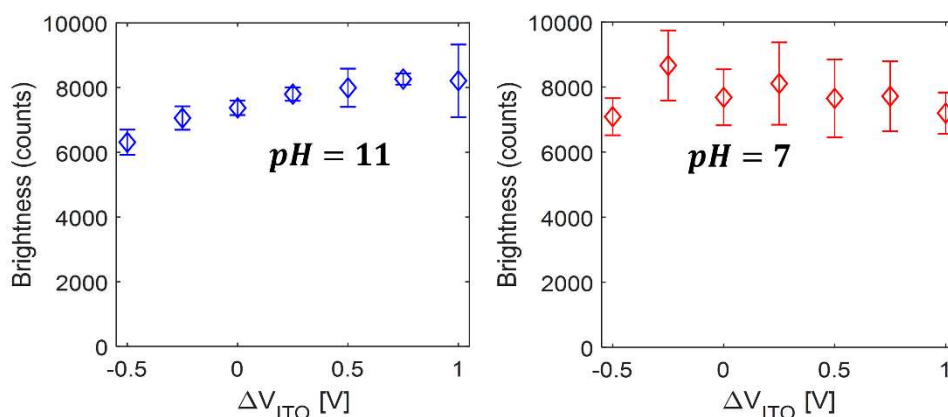
Figure S10. Voltage dependent mean brightness and its standard deviation show a slight increase in brightness with more positive voltages at pH=11, with negligible fluctuations. At pH=7, the fluctuations are much more significant, and no trend is observed for their brightness.

226   **Effect of ionic strength on interfacial dynamics.** To investigate the role of ionic

227   strength in the observed trends, the time-resolved fluorescence experiments described

228   above were repeated after replacing the solution in the flow cell with buffered electrolytes

229   with an ionic strength of 50 mM, for both pH values (pH=11 and pH =7, **Fig. S11**).
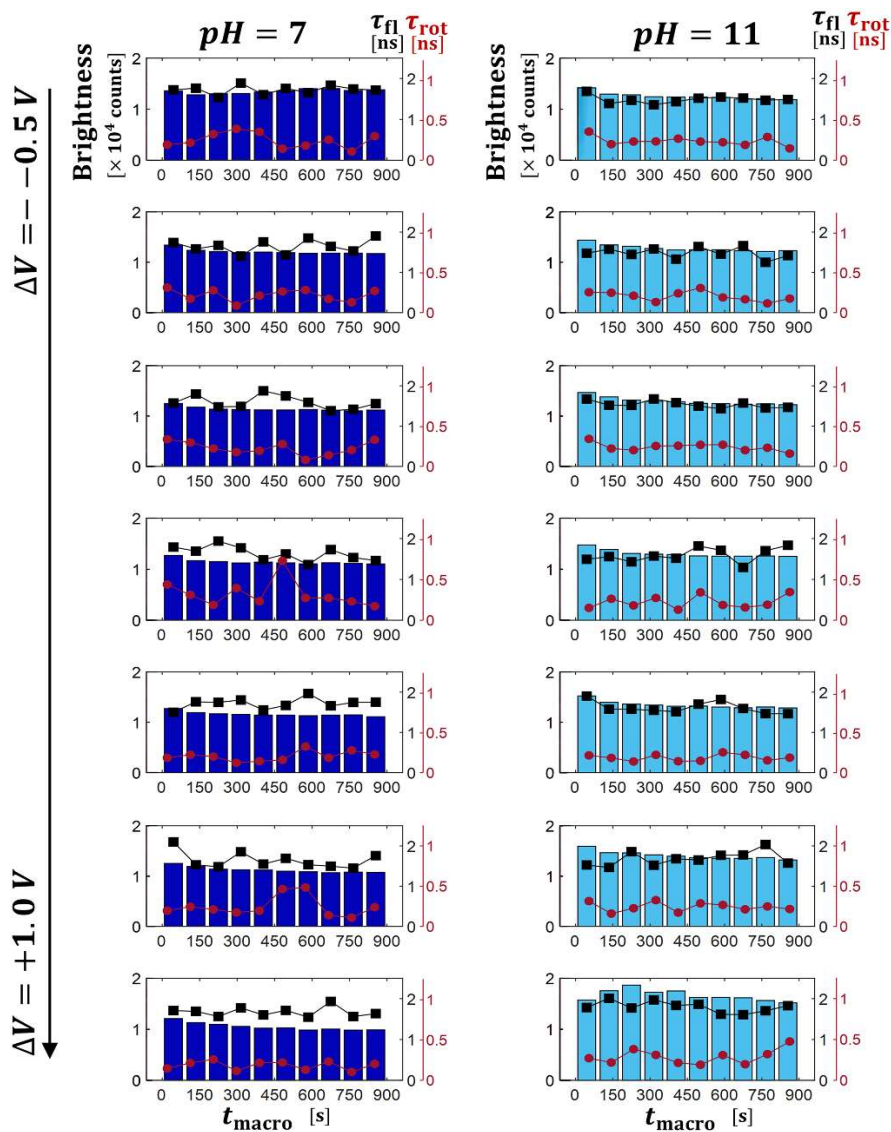
Figure S11. **Low ionic strength behavior of the time-resolved photoluminescence of adsorbed FITC-PLL on ITO as a function of voltage and pH,** equivalent to data for high ionic strength solutions in **Fig. 3**. Brightness trends for FITC-PLL adsorbed on ITO as a function of interfacial voltage while submerged in a pH=7 buffer (left), or a pH=11 buffer (right). Bars represent brightness, black squares are the fluorescence lifetime, and red circles are rotational diffusion time.

230 At this lower ionic strength, FITC-PLL adsorbates in contact with low- or high-pH solutions

231 display a low amplitude of fluctuations (< 20%). Similar to the data in high ionic strength

232 solutions, the applied electric field affects the photophysics of high pH samples, with little

233 effects on the properties of samples at low pH (**Fig. S12**).
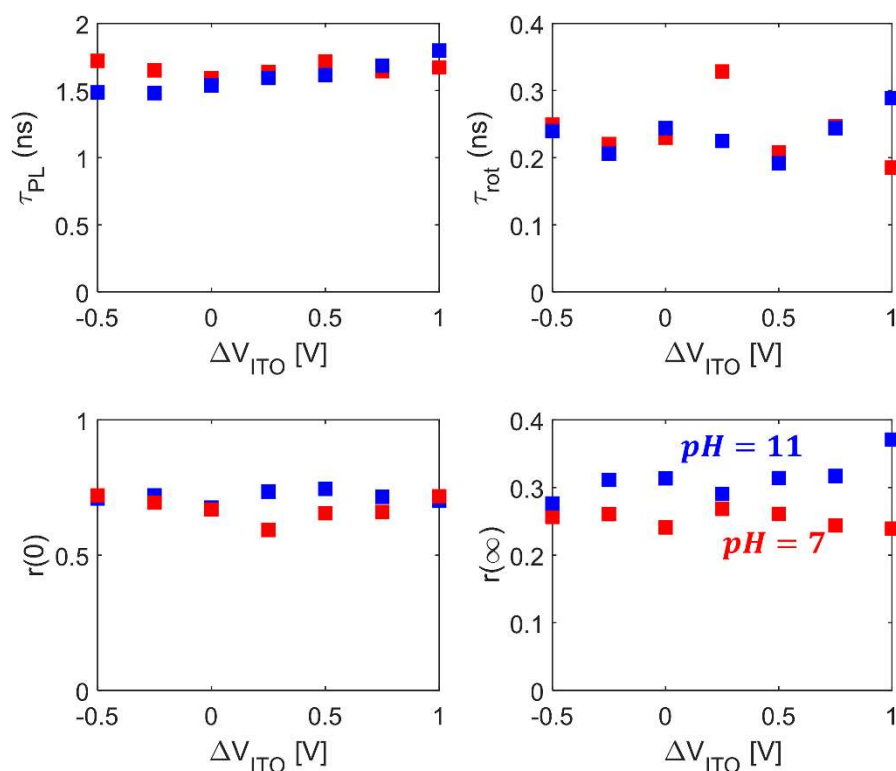
Figure S12. **At lower ionic strength, the voltage dependent photophysics of FITC-PLL** display a slight increase in fluorescence lifetime τ_{PL} and asymptotic anisotropy value $r(\infty)$ as voltage increases at pH=11. All other parameters show no voltage dependence. Plots show the average values for each voltage; blue markers are data at pH=11, red markers are data at pH=7. Buffer ionic strength for these experiments was 50 mM.

234

235

236 **<u>Safety and Hazards statement.</u>** Hazards associated with this work are primarily due to

237 the use of non-ionizing radiation (Class IV laser systems), as well as high power electrical

238 equipment (DC magnetron sputtering).

239

References.

(1) Park, J. H.; Buurma, C.; Sivananthan, S.; Kodama, R.; Gao, W.; Gessert, T. A. The Effect of Post-Annealing on Indium Tin Oxide Thin Films by Magnetron Sputtering Method. *Applied Surface Science* **2014**, *307*, 388–392. https://doi.org/10.1016/j.apsusc.2014.04.042.

(2) Wu, W.-F.; Chiou, B.-S.; Hsieh, S.-T. Effect of Sputtering Power on the Structural and Optical Properties of RF Magnetron Sputtered ITO Films. *Semicond. Sci. Technol.* **1994**, *9* (6), 1242–1249. https://doi.org/10.1088/0268-1242/9/6/014.

(3) Kim, H.; Horwitz, J. S.; Kushto, G.; Piqué, A.; Kafafi, Z. H.; Gilmore, C. M.; Chrisey, D. B. Effect of Film Thickness on the Properties of Indium Tin Oxide Thin Films. *Journal of Applied Physics* **2000**, *88* (10), 6021–6025. https://doi.org/10.1063/1.1318368.

(4) Ray, S.; Banerjee, R.; Basu, N.; Batabyal, A. K.; Barua, A. K. Properties of Tin Doped Indium Oxide Thin Films Prepared by Magnetron Sputtering. *Journal of Applied Physics* **1983**, *54* (6), 3497–3501. https://doi.org/10.1063/1.332415.

(5) Bender, M.; Seelig, W.; Daube, C.; Frankenberger, H.; Ocker, B.; Stollenwerk, J. Dependence of Oxygen Flow on Optical and Electrical Properties of DC-Magnetron Sputtered ITO Films. *Thin Solid Films* **1998**, *326* (1), 72–77. https://doi.org/10.1016/S0040-6090(98)00521-5.

(6) Mongay, C.; Cerda, V. A Britton-Robinson Buffer of Known Ionic Strength. *Analli di Chim.* **1974**, *64*, 409–412.

(7) *CRC Handbook of Chemistry and Physics*, 97th ed.; Haynes, W. M., Lide, D. R., Bruno, T. J., Eds.; CRC Press: Boca Raton.

(8) Synowicki, R. A. Spectroscopic Ellipsometry Characterization of Indium Tin Oxide Film Microstructure and Optical Constants. *Thin Solid Films* **1998**, *313–314*, 394–397. https://doi.org/10.1016/S0040-6090(97)00853-5.

(9) Brewer, S. H.; Franzen, S. Optical Properties of Indium Tin Oxide and Fluorine-Doped Tin Oxide Surfaces: Correlation of Reflectivity, Skin Depth, and Plasmon Frequency with Conductivity. *Journal of Alloys and Compounds* **2002**, *338* (1), 73–79. https://doi.org/10.1016/S0925-8388(02)00217-7.

(10) Brewer, S. H.; Franzen, S. Indium Tin Oxide Plasma Frequency Dependence on Sheet Resistance and Surface Adlayers Determined by Reflectance FTIR Spectroscopy. *J. Phys. Chem. B* **2002**, *106* (50), 12986–12992. https://doi.org/10.1021/jp026600x.

(11) Moutzouris, K.; Papamichael, M.; Betsis, S. C.; Stavrakas, I.; Hloupis, G.; Triantis, D. Refractive, Dispersive and Thermo-Optic Properties of Twelve Organic Solvents in the Visible and near-Infrared. *Appl. Phys. B* **2014**, *116* (3), 617–622. https://doi.org/10.1007/s00340-013-5744-3.

(12) Hale, G. M.; Querry, M. R. Optical Constants of Water in the 200-Nm to 200-Mm Wavelength Region. *Appl. Opt., AO* **1973**, *12* (3), 555–563. https://doi.org/10.1364/AO.12.000555.

(13) Weber, M. J. *Handbook of Optical Materials*; 2003.

(14) Optical Glass Data Sheets. SCHOTT.

(15) Mathar, R. J. Refractive Index of Humid Air in the Infrared: Model Fits. *J. Opt. A: Pure Appl. Opt.* **2007**, *9* (5), 470–476. https://doi.org/10.1088/1464-4258/9/5/008.

(16) Handelman, A.; Apter, B.; Shostak, T.; Rosenman, G. Peptide Optical Waveguides. *Journal of Peptide Science* **2017**, *23* (2), 95–103. https://doi.org/10.1002/psc.2944.

287   (17) Zhao, H.; Brown, P. H.; Schuck, P. On the Distribution of Protein Refractive Index
288   Increments. *Biophys J* **2011**, *100* (9), 2309–2317.
289   https://doi.org/10.1016/j.bpj.2011.03.004.
290   (18) Mirtič, A.; Grdadolnik, J. The Structure of Poly-l-Lysine in Different Solvents.
291   *Biophysical Chemistry* **2013**, *175–176*, 47–53.
292   https://doi.org/10.1016/j.bpc.2013.02.004.
293